Journal of Physics:
Condensed Matter

PAPER • OPEN ACCESS

Electronic and vibrational properties of interstitial clusters in degenerately boron-doped silicon

To cite this article: K Dhamotharan *et al* 2025 *J. Phys.: Condens. Matter* **37** 465901

OPEN ACCESS
IOP Publishing
Journal of Physics: Condensed Matter
J. Phys.: Condens. Matter **37** (2025) 465901 (12pp)
https://doi.org/10.1088/1361-648X/ae191e

Electronic and vibrational properties of interstitial clusters in degenerately boron-doped silicon

K Dhamotharan[1], S Wang[2,3], S P Hayes[1], Q M Ramasse[2,3], L J Phillips[4], J D Major[4], G Zoppi[5], S J Clark[1] and B G Mendis[1,*]

[1] Department of Physics, Durham University, Durham DH1 3LE, United Kingdom
[2] SuperSTEM Laboratory, SciTech Daresbury Campus, Daresbury WA4 4AD, United Kingdom
[3] School of Chemical and Process Engineering, University of Leeds, Leeds LS2 9JT, United Kingdom
[4] Stephenson Institute for Renewable Energy, Department of Physics, University of Liverpool, Liverpool L69 7ZF, United Kingdom
[5] Department of Mathematics, Physics and Electrical Engineering, Northumbria University, Newcastle Upon Tyne NE1 8ST, United Kingdom

E-mail: b.g.mendis@durham.ac.uk

Received 27 August 2025, revised 15 October 2025
Accepted for publication 29 October 2025
Published 13 November 2025

Abstract

Degenerate boron-doped silicon is prone to interstitial clustering, which adversely impacts key electrical properties, such as carrier concentration and mobility. Clustering becomes increasingly important with device miniaturisation, due to the high boron concentrations involved. Here we use vibrational and Compton electron energy-loss spectroscopy (EELS) in a (scanning) transmission electron microscope to measure changes in the vibrational and electronic properties of the silicon host lattice due to degenerate boron doping ($10^{20}\,\mathrm{cm}^{-3}$ hole concentration). A broad phonon defect band centred at $1064\,\mathrm{cm}^{-1}$ wavenumber was detected. Subtle changes in bonding anisotropy due to boron doping along [110] and [100] directions were also observed. Density-functional-theory modelling showed that boron acceptors had very little effect on the phonon and bonding properties. Instead boron interstitial clusters two to three atoms in size produce changes that agree more closely with experiment. However, the limited vibrational EELS energy resolution and background thermal diffuse scattering artefacts in Compton profiles do not allow a precise identification of the numerous cluster configurations that could potentially form. The results nevertheless suggest the potential of using high-spatial-resolution EELS for the detection of clustering phenomena at the device level.

---

[*] Author to whom any correspondence should be addressed.

Supplementary material for this article is available online

Keywords: vibrational electron energy-loss spectroscopy, electron Compton scattering, phonon defect modes, bonding anisotropy, degenerate boron-doped silicon

---

1. Introduction

Boron doping in silicon is critical in the semiconductor industry, in particular for fabrication of sub-micrometer and nanometer-scale electronic devices. In these miniaturised systems, precise control over the concentration and distribution of dopants is important for ensuring optimal device performance. However, in regions where the boron concentration exceeds the solubility limit (approximately $5\times10^{20}\text{cm}^{-3}$ at 900°C [1]), boron atoms exhibit non-ideal behaviour, such as precipitation and clustering [2, 3]. These clusters, often referred to as boron interstitial clusters (BICs), lead to complex activation and diffusion phenomena [4], making their study essential for understanding how they impact device reliability and performance. For example, in the development of CMOS devices, achieving junction depths of ~540 Å for 0.18 μm devices and down to 300 Å for 0.10 μm devices requires exceeding the solubility limit of boron [5]. The formation of boron clusters arises as a consequence of these high doping concentrations by the combined processes of high-dose ion implantation and rapid thermal processing, which can severely affect the device's electrical characteristics as clusters might remain electrically inactive [6].

Identifying the most prevalent BICs in silicon can significantly aid in designing effective fabrication strategies to address their impact on device performance. While several studies have highlighted the potential effects of BICs on semiconductor functionality [7–15], there remain significant gaps in accurately characterising these clusters, and understanding their vibrational modes and electronic structure, which could reveal both beneficial and detrimental aspects of BICs. Furthermore, despite the growing demand for highly doped shallow junctions that exceed the solubility limit, there has been limited research into the boron clustering that takes place under conditions of high boron supersaturation [16]. A promising approach to bridge these gaps involves comparing the calculated vibrational and electronic properties of various boron complexes with those observed experimentally in silicon. By integrating advanced techniques such as density functional theory (DFT) [17, 18] and electron microscopy, we can make semi-quantitative predictions about both electronic and vibrational properties. Focusing on these characteristics of BICs provide deeper insights into how these clusters form, evolve, and ultimately influence device behaviour.

In this study, we have investigated both the vibrational and electronic properties of degenerately boron-doped silicon to gain a comprehensive understanding of BICs. To investigate vibrational properties, we used aberration-corrected scanning transmission electron microscopy (STEM) combined with monochromated electron energy loss-spectroscopy (EELS) to obtain phonon frequencies. This technique has recently detected phonon defect modes due to a single impurity atom in a 2D material [19] and is therefore a suitable choice for characterising BICs embedded in a 3D crystal lattice. For the electronic properties, electron Compton scattering was performed using transmission electron microscopy (TEM). Compton scattering is a well-established technique for determining the electron momentum distribution in the ground state of solids [20]. Although typically performed using x-rays, this technique has more recently been expanded to high-energy electron beams and can be performed using a TEM. Compton scattering has been used to investigate bonding anisotropy in solids [21–23], but has yet to be applied to studying dopants in semiconductors. The strong interaction of an electron beam with the specimen enables high sensitivity, such as detecting ~0.1% electron density change in a 2D material [22]. To complement the experimental findings, we also performed DFT simulations to calculate the phonon and electronic structure. This comprehensive analysis allows us to correlate experimental observations with theoretical models, offering deeper insights into BICs in silicon.

2. Computational methods

Electronic and phonon properties of supercells containing 64 and 216 tetrahedrally bonded silicon atoms with boron point defects were simulated using plane-wave pseudopotential DFT, as implemented in Castep [24, 25]. Norm-conserving pseudopotentials were used, and the local density approximation (LDA) to describe exchange correlation interactions [26–28]. A plane-wave cutoff energy of 500 eV and $2\times2\times2$ Monkhorst–Pack k-point grid was applied [29] giving total energy convergence to better than 1 meV/atom (see supplementary material). Boron point defect configurations included substitutional acceptor ions, and neutral interstitials as isolated atoms and clusters. During geometry optimisations, the lattice parameters and cell angles were fixed only for the BICs with 64 atoms, allowing only the atomic positions to relax. This was done to avoid an unrealistic supercell structure, that could arise from excessive distortion in the lattice due to periodic boundary conditions and interaction between neighbouring clusters. The relaxation process for all systems continued until the residual force on each atom was less than $0.05\,\text{eV}\text{Å}^{-1}$, the energy difference between consecutive ionic relaxation steps per ion was below 5×10^{-5} eV, and the maximum displacement was below 1×10^{-3} Å.

Defect formation energy (E_f): The defect formation energy E_f was calculated following the formalism in [30] to identify the energetically favourable BICs in silicon:

$$E_f = E^T_{\text{defect}} - E^T_{\text{perfect}} - \sum_i n_i \mu_i + qE_F, \tag{1}$$

where, E^T_{defect} and E^T_{perfect} are the total energies of the supercell with and without the defect, respectively. n_i represents the number of atoms of species i (chemical potential μ_i) added to or removed from the supercell. The term q indicates the charge on the defect, and E_F is the Fermi energy. The chemical potential for silicon was calculated as $\mu_{\text{Si}} = E^T_{\text{Si}}/N_{\text{Si}}$, where E^T_{Si} is the total energy of a silicon supercell with no defects and N_{Si} is the number of silicon atoms. Similarly, the chemical potential for boron was defined as $\mu_{\text{B}} = E^T_{\text{B}}/N_{\text{B}}$, where E^T_{B} is the total energy of the rhombohedral boron primitive cell and N_{B} is the number of boron atoms.

Phonon calculation: Phonon frequencies were simulated using density-functional-perturbation methods [31] for various boron configurations. The supercell dimensions were set to 1 × 1 × 1, with the dispersion path chosen from the Γ point to the X point in the Brillouin zone. Phonon wavenumbers for the 216 atom supercell with defect were deemed converged, and showed only small (∼10-20 cm^{-1}) differences compared to the 64 atom results. As further confirmation of convergence, phonon calculations were also performed for a 512 atom supercell containing a single boron point defect in substitutional and interstitial configurations, and produced almost identical results. The aim of phonon simulations was to identify potential boron defect configurations with phonon wavenumbers close to the experimentally observed value of 1064 cm^{-1}, which is well above the optical phonon mode (516 cm^{-1}) for elemental silicon. The 64 atom supercell was therefore chosen as the default DFT supercell size, since it produced the same trends as the 216 atom supercell, with only minor numerical differences in phonon wavenumber. Furthermore, any strain was confined to within a few nearest neighbours of the boron atom(s) and was negligible at the edges of a 64 atom supercell. The computational efficiency of a smaller supercell enabled a larger number of defect configurations to be explored without compromising the underlying physics. All DFT results reported in this paper are therefore for a 64 atom supercell.

Compton profiles: Compton scattering is usually understood as a two-body collision between a particle (photon or high energy electron) and stationary free electron, with energy transfer depending on the scattering angle. However, electrons in a material have momentum and so this leads to a Doppler broadening effect that results in a broadened energy spectrum rather than a single value. The broadened profile is known as the Compton profile, which is measured experimentally. The double-differential scattering cross section (DDSCS) for Compton scattering is given as follows [32]:

$$\frac{\mathrm{d}^2\sigma}{\mathrm{d}E\mathrm{d}\Omega} \propto J(p_z)\,. \tag{2}$$

where σ is the cross section, E is the energy transfer and Ω is the scattering solid angle. $J(p_z)$ is the Compton profile given by:

$$J(p_z) = \iint n(p_x, p_y, p_z)\,\mathrm{d}p_x\,\mathrm{d}p_y, \tag{3}$$

where $n(\mathbf{p})$ is the ground state electron momentum density. By convention, the scattering vector $\mathbf{q}$ is taken to be along the z-direction, i.e. parallel to the p_z component of the electron momentum $\mathbf{p}$. The Compton profile is therefore the projection of the electron momentum density along the scattering vector. The ability to access the ground-state electron momentum density directly relies upon satisfying the impulse approximation, which requires that the energy transfer be much greater than the electron binding energy [32]. This ensures that the bound electron can effectively be treated as being 'free', whilst having the momentum distribution of an electron in the solid.

Equation (3) shows that the Compton profile can be calculated from the electron momentum density. Castep uses a plane-wave basis set which allows the real space wavefunction to be represented as a Fourier series. The momentum-space wavefunction can be obtained through a Fourier transform. The momentum density is simply the modulus-squared of this wavefunction and can be expressed as:

$$n(\mathbf{p}) = \sum_{n,\mathbf{k},\mathbf{G}} f_{n,\mathbf{k}} |C_{n,\mathbf{k},\mathbf{G}}|^2 \delta(\mathbf{k}+\mathbf{G}-\mathbf{p})\,, \tag{4}$$

where n labels the electronic bands, $\mathbf{k}$ labels the k-points in the Brillouin zone and $\mathbf{G}$ represents the reciprocal lattice vectors used in the Fourier series [33]. The k-point sampling is taken to be the same as used for ensuring calculation convergence. $f_{n,\mathbf{k}}$ is the occupation function taking either 0 or 1 depending on whether the band is unoccupied or occupied respectively. $C_{n,\mathbf{k},\mathbf{G}}$ are the Fourier coefficients. The delta function selects only those Fourier coefficients that contribute to $n(\mathbf{p})$.

The Compton profile DFT calculations used a 64 atom unit cell. Phonon simulations indicate that this supercell size is sufficient to minimise artefacts due to periodic finite size effects. However, for accurate momentum densities $J(p_z)$ the supercell size must be chosen so that the correct boron concentration is reproduced. For a single boron acceptor in a 64 atom supercell the boron concentration is 8×10^{20}cm^{-3}, nearly an order of magnitude larger than the 10^{20}cm^{-3} hole concentration measured by the Hall technique in our sample (section 3). BICs will increase the concentration even further. The effects of concentration are discussed in more detail in section 4. Since Castep employs pseudopotentials, only the valence Compton profile can be calculated. To model the core electron contribution to $J(p_z)$, Hartree–Fock free atom Compton profiles were used [34].

3. Experimental methods

Degenerate boron-doped silicon was commercially sourced from University Wafer Inc. Secondary ion mass spectroscopy (SIMS) confirmed the presence of boron doping, while Hall measurements indicated an approximately constant hole concentration of $10^{20}\,\mathrm{cm}^{-3}$ within the 10 K–320 K temperature range (see supplementary material). It is therefore concluded that the semiconductor is in the saturation regime at room temperature and the boron acceptors are fully ionised. Elemental silicon was purchased from Sigma Aldrich and was used as a reference to evaluate changes in the physical properties due to boron doping. Electron transparent samples along the <100>, or in some cases <110>, zone-axis were prepared using a FEI Helios 600 focused ion-beam (FIB) microscope. STEM-EELS data were acquired at 60 kV using the Nion Ultra STEM 100 MC microscope [35] at the SuperSTEM Laboratory, equipped with a Nion Iris EELS spectrometer and Dectris ELA hybrid-pixel direct electron detector. This setup, featuring an ultra-high energy resolution electron beam monochromator, is particularly effective for vibrational EELS measurements, enabling the detailed investigation of phonon modes due to dopants [36]. EELS spectra were acquired in both on-axis and off-axis collection geometries (see supplementary material). For the latter the bright-field transmitted disc was deflected by 55 mrad with respect to the EELS spectrometer aperture. Since the zero loss peak (ZLP) intensity is lower, the peak-to-background ratio of any phonon modes is improved. The 30.5 mrad probe semi-convergence angle was sufficiently large to potentially excite all phonon modes within the first Brillouin zone for silicon. The EELS collection semi-angle was 44 mrad and 22 mrad for on-axis and off-axis geometries, respectively. A 10 ms (on-axis) and 30 ms (off-axis) acquisition time per frame was employed to balance energy resolution and signal-to-noise ratio. A total of 210 000 (on-axis) and 60 000 (off-axis) frames are aligned to correct for any drift in the ZLP and then summed to produce a cleaner spectrum. The effective energy resolution, as estimated by the ZLP full-width-at-half-maximum (FWHM) for the STEM probe incident on the specimen, was 12 meV and 14 meV for the on-axis and off-axis spectra, respectively. The dispersion was 1.2 meV/channel.

Electron Compton measurements were carried out in a JEOL 2100F FEG TEM at 200 kV. A Gatan Tridiem EELS spectrometer was used for recording the Compton spectra at 0.5 eV/channel dispersion in centred dark-field image mode. The objective aperture 'radius' corresponds to 5.3 mrad scattering angle. The Compton profiles were measured with 1.6–1.7 $\mathrm{\AA}^{-1}$ scattering vector magnitude along [110] and [100] crystal directions. For accurate results Bragg scattering before and after the Compton event must be minimised [37]. The specimen was therefore tilted away from the <100> or <110> zone-axis along the appropriate Kikuchi band (220 or 004). The tilt angle for the elemental silicon sample was $7^{\mathrm{o}}-8^{\mathrm{o}}$, while the boron-doped silicon sample had a slightly smaller tilt angle of $4^{\mathrm{o}}-5^{\mathrm{o}}$, although this was still sufficient to minimise Bragg diffraction spots from the zone-axis. The specimen orientation nominally satisfied two-beam diffraction conditions, with a positive deviation parameter to further minimise the diffracted beam intensity [38]. The thickness of both specimens was estimated using EELS to be 0.8 inelastic mean free paths (~700 Å) at 200 kV accelerating voltage. Similar thicknesses were deliberately chosen to minimise any specimen related artefacts, such as (elastic) Bragg and (phonon) thermal diffuse scattering (TDS). In EELS a power law background subtraction method is usually employed; however, for the large energy loss region a typical Compton profile extends over it gives inaccurate results [39]. Instead, an empirical background subtraction routine was employed by acquiring a 'bright-field' EELS spectrum at small scattering angles and kinematic diffraction conditions [40]. This bright-field EELS spectrum has the Compton signal suppressed, so that suitably normalised inelastic scattering distributions can be used to subtract the background and core-loss edges from the Compton profile present in the dark-field EELS spectrum. This has been successfully employed in silicon before [40] and so was the obvious method of choice here. The intensity of the background subtracted Compton profile is proportional to $J(p_z)$. The energy-loss axis in the EELS spectrum can be converted to electron momentum p_z through a simple expression under the impulse approximation given by [41]:

$$p_z = -\delta E\sqrt{\frac{m_e}{2E_p}}, \qquad (5)$$

where m_e is the electron rest mass, E_p is the peak energy-loss of the Compton event as given by the case for a stationary electron and δE refers to the difference in energy loss from E_p due to the Doppler broadening [41]. p_z is reported in atomic units (a.u.) throughout this paper.

4. Results and discussion

4.1. EELS vibrational spectroscopy and DFT simulations

The phonon EELS spectrum for boron-doped silicon was dominated by the optical mode of the host silicon lattice at 64 meV. Since boron is lighter than silicon, any defect phonon modes due to doping are expected at higher energies [42]. For brevity, results are presented only for the off-axis EELS measurements; analysis of the on-axis data gave similar conclusions and can be found in the supplementary material. The off-axis EELS spectrum for boron-doped silicon in figure 1(a) shows additional intensity above the power law fitted background [43] in the ~100–200 meV energy loss range. Since this is a larger energy than the 64 meV optical mode for silicon, it is likely due to lighter element impurities in the sample, such as boron dopants. There is also weaker additional intensity above ~250 meV, which is attributed to phonon modes from hydrocarbons that accumulate on the specimen surface during prolonged STEM-EELS measurements. The off-axis EELS spectrum acquired from the elemental silicon sample is shown in figure 1(b). Extra phonon intensity due to light atom impurities (~100–200 meV energy loss range) as well as surface contamination (above ~250 meV) is present for this sample as well. Although there is no intentional doping, light elements such as carbon, oxygen and nitrogen are still present as residual impurities in electronics grade silicon [44]. The impurity phonon band appears more evenly distributed in elemental silicon, while for boron-doped silicon the centre of mass has shifted

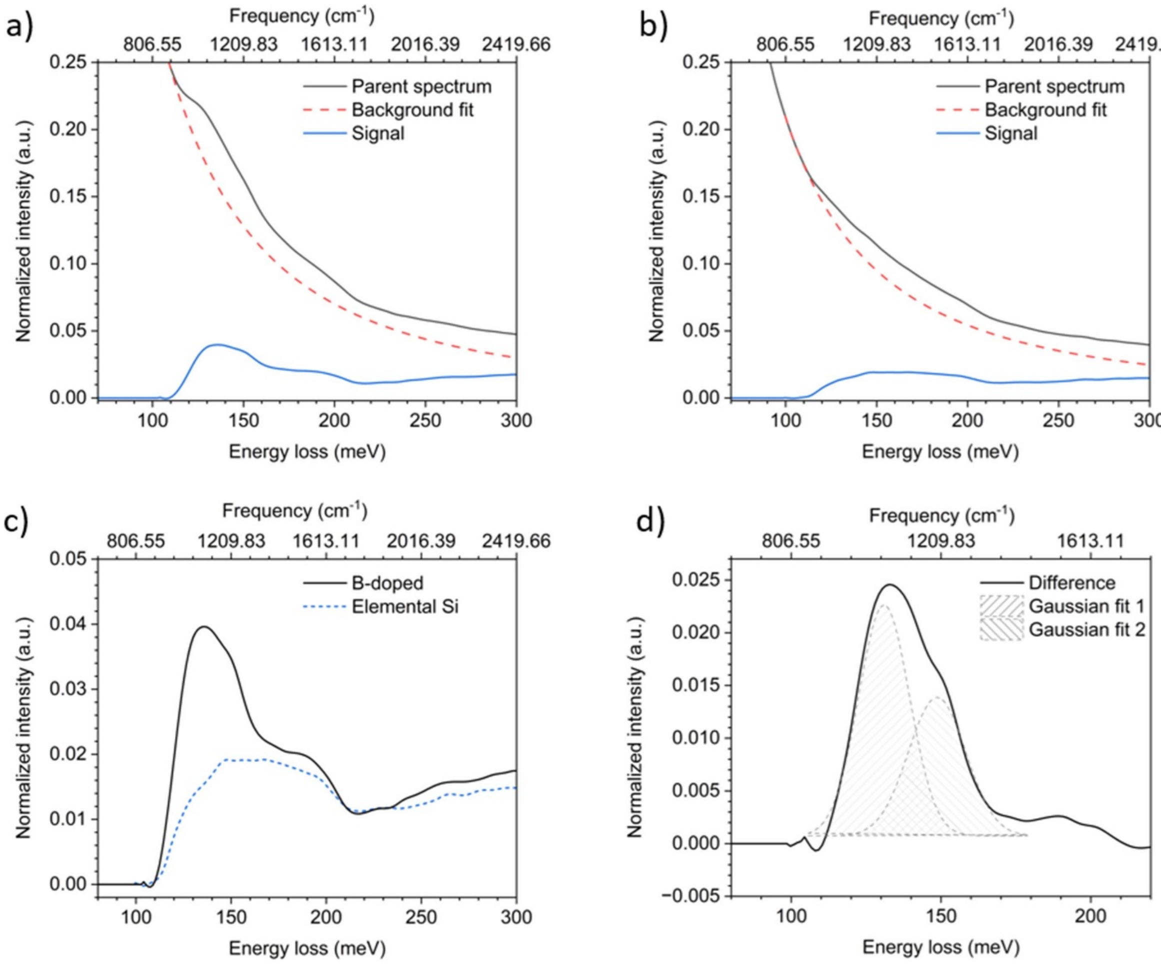

Figure 1. Off-axis EELS spectra for (a) boron-doped silicon and (b) elemental silicon at energy losses above the silicon optical phonon mode. The defect phonon signal is extracted by modelling the underlying background using a power law function. The defect phonon signal for the two specimens are shown superimposed in (c). Their difference is plotted in (d). Two Gaussians are fitted to the main peak of the difference profile. In all figures the EELS spectrum has been Fourier-log deconvolved and the intensity of the silicon optical phonon mode normalised for direct comparison.

to lower energies. These changes are likely due to boron doping, whose effects are superimposed on the phonon spectrum from other impurities intrinsic to silicon.

The vibrational changes due to boron doping are evaluated by using the EELS spectrum for elemental silicon as a reference. This requires suitably normalising the impurity phonon intensity for the two samples and calculating their difference. It is important to correct for any variations in thickness between the two specimens. This is done by extracting the single inelastic scattering distribution through a Fourier-log deconvolution [43]. Strictly speaking, Fourier-log deconvolution is normally applied to the full energy loss spectrum, whereas the limited energy range in high dispersion, vibrational EELS spectra means that other important inelastic events, such as plasmon scattering, are not measured. However, these inelastic signals have higher energies than phonons, so that the Fourier-log method can still be used to obtain a single phonon scattering distribution, which is valid for energy losses in the (pre-plasmon) meV energy range. Following Fourier-log deconvolution the intensity of the 64 meV silicon optical phonon mode was normalised. This results in a common intensity scale for spectra acquired under different experimental conditions. The impurity phonon signal is extracted by fitting the underlying background to a power law model. The impurity phonon signal for the two specimens are shown superimposed in figure 1(c), while figure 1(d) plots their difference. The main peak of the difference spectrum is least squares fitted to two Gaussian distributions, centred at 132 meV and 149 meV, respectively. The smaller peak at 149 meV is assumed to be due to differences in impurity levels of silicon feedstock used by the different manufacturers of elemental silicon and boron-doped silicon samples (section 3). The larger peak at 132 meV is likely caused by changes in vibrational properties due to boron doping. The FWHM of the 132 meV Gaussian peak was 21 meV, which is larger than the 14 meV effective energy resolution of the off-axis EELS measurement. This suggests a range of different phonon mode energies associated with boron doping.

A FIB prepared TEM sample will inevitably form a fresh SiO_x oxide layer on the surface when exposed to air, which can be confirmed by the presence of an O K-edge in the EELS spectrum (see supplementary material). The native

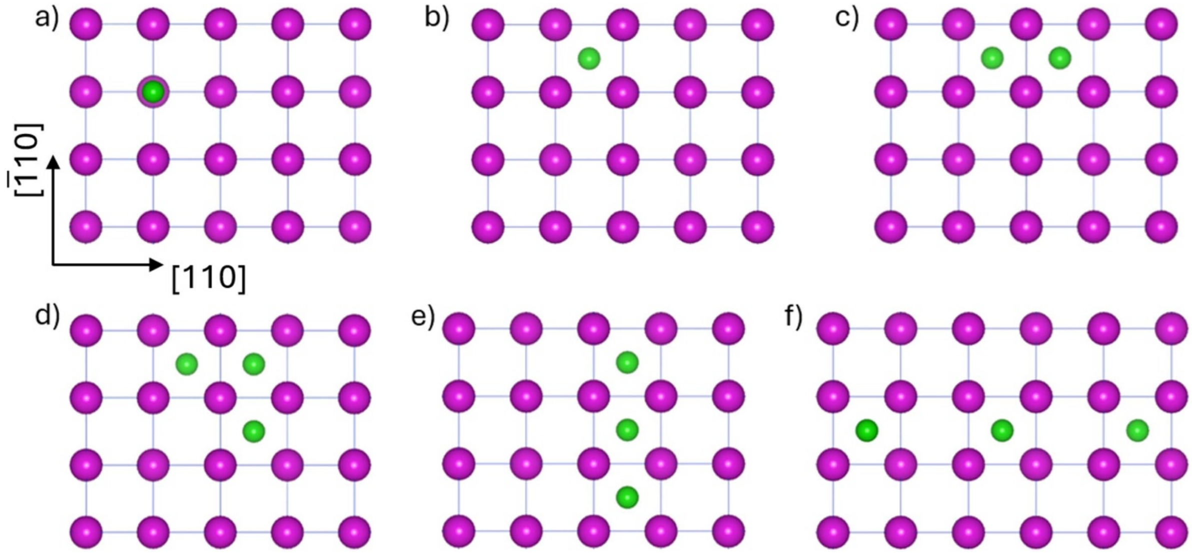

Figure 2. Structural configurations of boron defects in silicon as viewed along [001]. Green and violet atoms represent boron and silicon atoms, respectively. (a) Boron acceptor (B^-) defect corresponds to a single boron atom incorporated into the silicon lattice. (b) The neutral boron interstitial defect (B_i^0) represents a single boron atom in an interstitial position within the lattice. (c) The boron interstitial cluster ($2B_i^0$) with two neutral boron atoms in interstitial sites. (d) Boron interstitial cluster ($3B_i^0$—confi 1) with three neutral boron atoms illustrates a tightly bound trio of interstitials. (e) Boron interstitial cluster ($3B_i^0$—confi 2) shows three neutral boron atoms arranged in a linear fashion, forming a less compact structure. (f) Boron interstitial cluster ($3B_i^0$—confi 3) shows a linear arrangement with alternating boron interstitial atoms and empty interstitial spaces.

oxide is self-limiting at ~2 nm thickness [45]. The asymmetric Si–O–Si stretch mode in bulk SiO_x has wavenumbers that overlap with the experimentally observed phonon defect band [46]. The vibronic peaks of a silicon surface exposed to air at room temperature however have very weak intensity and are extremely broad [47]. Annealing the specimen at 700 K for 1 min produced sharper peaks and an overall spectrum that matched more closely with bulk SiO_x. It has been proposed that the initial broad peaks are due to a smaller Si–O–Si bond angle in a highly compressed native oxide layer that is formed at room temperature [47]. Since the FIB-TEM samples did not undergo any further annealing treatment we expect any signal due to asymmetric Si–O–Si stretch modes to be suppressed. Furthermore, when calculating a difference spectrum between boron-doped silicon and elemental silicon, such as in figure 1(d), the contribution from any surface oxide layers approximately cancel, leaving behind the signal due to boron doping. Several boron point defect configurations were therefore explored with the aim of identifying, through DFT the origin of the EELS phonon defect intensity at 132 meV (1064 cm^{-1}). It is assumed that boron dopants alone are responsible for this defect peak, i.e. any surface oxide layer contributions are minimal and any interaction between boron and other impurities within the sample can largely be ignored. This is reasonable considering the sample shows degenerate p-type extrinsic behaviour, as confirmed by Hall measurements. The boron concentration must therefore be larger than the intrinsic impurity level.

Boron defect supercells are shown in figure 2, while table 1 lists their formation energies (3D projections of the supercells can be found in the supplementary material). Isolated point defects include the ionised boron acceptor (B^-) occupying substitutional sites, as well as both neutral (B_i^0) and charged (B_i^-) boron interstitials. The interstitial was placed at the midpoint of a silicon nearest-neighbour tetrahedron edge. A supercell with two nearest-neighbour, ionised acceptors (i.e. $2B^-$) was also simulated. BICs are denoted by XB_i^0, and consists of X number of neutral boron atoms. The boron interstitials were all clustered on the same $(10\bar{1})$ crystallographic plane. Cluster sizes of $X = 2$ and 3 boron atoms were simulated, the latter in three different configurations (figures 2(d)–(f)). The three configurations exhibit decreasing levels of interstitial packing density. For example, all three interstitials are confined to a single unit cell of silicon in configuration 1. The remaining two configurations have the three interstitials aligned along the $<111>$ direction, but with increasing spacing between the boron atoms, such that they span multiple unit cells. It should

Table 1. Formation energies of boron point defect configurations in silicon. Numbers within brackets denote the formation energy per atom.

Defect type	Defect formation energies (eV)
B^-	2.17
B_i^0	3.73
B_i^-	5.77
$2B^-$	5.19 (2.60)
$2B_i^0$	5.10 (2.55)
$3B_i^0$-confi 1	5.71 (1.90)
$3B_i^0$-confi 2	7.13 (2.38)
$3B_i^0$-confi 3	10.22 (3.41)

be emphasised that an exhaustive search of cluster configurations has not been carried out; instead, the aim is to identify the physical nature of point defects that give phonon wavenumbers in the ∼1064 cm^{-1} range, as observed by STEM-EELS. The limited energy resolution and low signal of vibrational EELS precludes identification of the exact defect configurations present in our sample.

The boron acceptor had the lowest formation energy for a single point defect (table 1). The energy of an isolated interstitial is significantly higher, indicating that at low concentrations boron predominantly occupies lattice sites, resulting in semiconductor doping. The formation energy is higher when the boron interstitial is ionised, and therefore all subsequent simulations assumed charge neutral boron interstititals. For very high boron concentrations, such as the degenerate doping in our samples, the average spacing between boron atoms is such that they can no longer be considered isolated. Under these conditions table 1 indicates that interstitial formation is favoured, i.e. the $2\mathrm{B}_i^0$ cluster in figure 2(c) has a lower formation energy than two nearest-neighbour acceptors. We expect this to be a general trend, since the mutual repulsion between B^- acceptors does not favour a small distance of separation. Increasing the cluster size from 2 to 3 atoms lowers the formation energy per atom even further, provided the boron atoms are closely packed within the cluster. For example, there is a direct correlation between formation energy and packing density for the three $3\mathrm{B}_i^0$ cluster configurations examined in this study. There are however limits to the size and packing density of the cluster that can be accommodated. Preliminary simulations on an octahedrally shaped $6\mathrm{B}_i^0$ cluster resulted in an even lower formation energy per atom (1.75 eV), but there was also significant local strain around the cluster following geometry optimisation.

The DFT simulated, vibrational wavenumbers for the different point defect configurations are summarised in table 2. For a system with N atoms, there are a total of $3N$ vibrational modes, consisting of three acoustic and $3(N-1)$ optical modes. Since boron is lighter than silicon, it only contributes to optical modes rather than acoustic ones. Table 1 therefore lists wavenumbers for the $3N_\mathrm{B}$ number of highest energy modes for each defect configuration, where N_B is the number of boron atoms in the defect. The defect modes are non-dispersive, i.e. the wavenumber is constant across the Brillouin zone. Note that all three defect modes for the B^- acceptor are degenerate, and therefore only one wavenumber is listed. The 632 cm^{-1} B^- mode is only slightly higher than the 516 cm^{-1} optical mode for elemental silicon, and cannot explain the high energy 1064 cm^{-1} defect modes observed by STEM-EELS. The 116 cm^{-1} wavenumber difference between B^- and silicon optical modes is similar to the effective EELS resolution (14 meV or 113 cm^{-1} ZLP FWHM), which may explain why these modes were not observed, despite a $10^{20}\mathrm{cm}^{-3}$ hole concentration measured by the Hall technique. For interstitial boron atoms, a broader and higher range of vibrational wavenumbers are observed, due to replacing the relatively stiff Si-B bonds with lighter mass boron atoms that are only weakly bonded. The maximum wavenumber generally increases with cluster size [12, 48, 49], provided the packing density is sufficiently high; for example, 840, 937 and 1015 cm^{-1} for B_i^0, $2\mathrm{B}_i^0$ and $3\mathrm{B}_i^0$ (configuration 1), respectively. The maximum wavenumber (825 cm^{-1}) for the $3\mathrm{B}_i^0$ configuration 3 is anomalously lower than the other two $3\mathrm{B}_i^0$ configurations. This is attributed to the reduced packing density of the boron interstitials, which effectively decouples the boron atoms from one another.

Table 2. Vibrational wavenumbers of boron point defect configurations in silicon. The defect phonon modes for a B^- acceptor are triply degenerate.

Defect type	Wavenumber (cm^{-1})
B^-	632
B_i^0	532, 770, 840
$2\mathrm{B}_i^0$	528, 548, 697 700, 733, 937
$2\mathrm{B}^-$	494, 525, 525, 586, 586, 619
$3\mathrm{B}_i^0$-confi 1	511, 515, 529, 563, 612, 708, 720, 949, 1015
$3\mathrm{B}_i^0$-confi 2	502, 507, 521, 538, 638, 709, 731, 895, 1212
$3\mathrm{B}_i^0$-confi 3	504, 507, 511, 524, 587, 652, 772, 793, 825

The maximum wavenumbers for $3\mathrm{B}_i^0$ configurations 1 and 2 are similar to the 1064 cm^{-1} peak wavenumber extracted from STEM-EELS. This suggests that in addition to dopant acceptor ions the specimen also contains interstitial clusters. The broad (170 cm^{-1} FWHM) Gaussian fit in figure 1(d) is consistent with the wide range of defect phonon wavenumbers for a given interstitial cluster (table 2), although it is likely that there are also multiple cluster sizes and configurations in our sample, which will also contribute to the broadening. A further complication is that not all defect modes will contribute equally to the EELS phonon spectrum. In fact, the oscillator strength depends on $\mathbf{q}\cdot\mathbf{e}$, where $\mathbf{q}$ and $\mathbf{e}$ are the scattering and phonon polarisation vectors, respectively [50]. Phonon modes with polarisation vector perpendicular to the sample plane cannot therefore be excited by the focussed STEM probe. The STEM-EELS measurements were performed with the specimen in the <100> orientation. Examination of the highest phonon frequencies for $3\mathrm{B}_i^0$ configurations 1 and 2 showed in-plane specimen vibration components (see supplementary material), meaning these modes will contribute to the experimental phonon defect band.

4.2. Compton scattering and electronic structure

The measured EELS Compton signal (figure 3(a)) has a peak maximum between ∼450 and 500 eV energy loss, and is superimposed on the silicon L-edge (∼99 eV) background. A small carbon K-edge signal at ∼280 eV is also visible, due to contamination build-up during the relatively long acquisition times. Since the Compton signal is above silicon L, but still below the K-edge, all electrons apart from the silicon $1s^2$ electrons undergo Compton scattering. The Compton signal also includes all electrons from any boron atoms, since the boron K-edge is at ∼190 eV energy-loss. Following background subtraction (section 3), the high-energy-loss side of the Compton signal was used to analyse the electron momentum

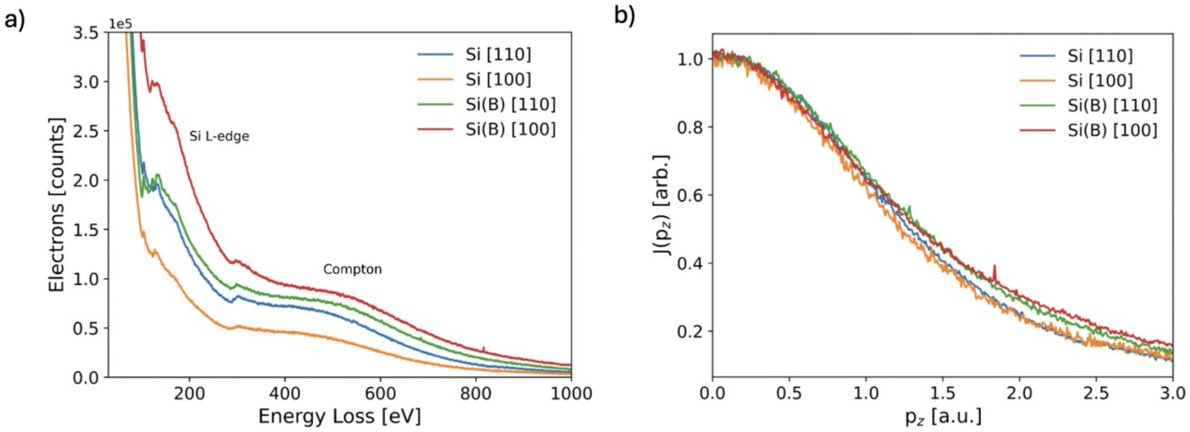

Figure 3. (a) Dark-field EELS Compton spectra for silicon and boron-doped silicon samples along [100] and [110] crystallographic directions. (b) Compton $J(p_z)$ profiles extracted after background subtraction, where the electron momentum density at $p_z = 0$ has been set to 1 for all profiles.

density. Since the area under the Compton profile is proportional to the number of electrons involved in the scattering (equation (3)), area normalisation is typically used when comparing two Compton profiles. For our measurements however this procedure cannot reliably be performed for two reasons. First the experimental Compton profiles were only measured to a momentum of ~3 a.u., so that $J(p_z)$ had not fully decreased to zero. Second the number of electrons undergoing Compton scattering in the boron-doped silicon sample is not accurately known. To overcome this, the Compton profile at $p_z = 0$ was normalised to unity. $J(p_z)$ curves along [110] and [100] directions for elemental Si and degenerate boron-doped Si samples are shown in figure 3(b). The Compton profiles for the boron-doped sample are slightly wider than elemental silicon.

Figure 4(a) shows $\Delta J(p_z)$ difference profiles between elemental Si and boron-doped Si, i.e. $\Delta J(p_z) = J(p_z)_{\mathrm{Si}} - J(p_z)_{\mathrm{Si(B)}}$. Profiles along [110] and [100] directions are plotted. Due to the normalisation procedure for $J(p_z)$, the difference profiles are forced to zero at $p_z = 0$. Beyond p_z ~0.5 a.u. $\Delta J(p_z)$ becomes negative, displaying a broad minimum between ~1.5-2.5 a.u momentum. Any anisotropy difference between [110] and [100] directions are within the noise level. When comparing experimental data to theory, care must be taken to account for the $J(0) = 1$ normalisation employed for the former. The following procedure was therefore adopted. The Castep valence $J(p_z)$ was area-normalised for the total number of $3s^2, 3p^2$ silicon and $2s^2, 2p^1$ boron valence electrons in the supercell. Next the Hartree–Fock $J(p_z)$ profiles for silicon $2s^2, 2p^6$ and $1s^2$ boron core electrons were area-normalised to the total number of each type of electron in the supercell. $1s^2$ silicon core electrons are omitted, since they do not undergo Compton scattering in our measurements. Summing the valence and core contributions gives the total $J(p_z)$ for the supercell, which is then normalised to unity at $p_z = 0$ for a direct comparison with experiment. A similar procedure is used for constructing $J(p_z)$ for elemental silicon.

Figure 4(b) shows theoretical $\Delta J(p_z)$ difference profiles between elemental Si and three defect configurations, namely B^- acceptor, B_i^0 single interstitial and $2B_i^0$ interstitial cluster. The change in $J(p_z)$ is measured along the [100] direction. The magnitude of $\Delta J(p_z)$ for acceptors is smaller than interstitials, although the latter is still an order of magnitude smaller than the experimental result (figure 4(a)). The boron concentration in the defect supercells are an order of magnitude larger than the $10^{20}\mathrm{cm}^{-3}$ hole concentration measured by the Hall technique (section 2). The hole concentration is equal to the ionised acceptor concentration and does not include interstitials, which are assumed to be charge neutral. In principle, it is therefore possible to increase the interstitial concentration in the DFT supercell still further by an order of magnitude, which should give better agreement with experiment. However, this is physically unrealistic, since the larger boron concentrations would introduce appreciable strain in the crystal lattice. Furthermore, the interstitial $\Delta J(p_z)$ show features that are not observed in experiment, such as a narrow maximum at p_z ~0.3 a.u and a narrow minimum at p_z ~0.7-0.8 a.u. Figures 4(c) and (d) plot the electron density change, i.e. difference in electron density between free atoms and when bonding is included, for a B_i^0 single interstitial and $2B_i^0$ interstitial cluster, respectively. Some anisotropy is observed, particularly for the interstitial cluster, where the electron density has accumulated between the boron atoms due to bonding within the cluster. Hence the $\Delta J(p_z)$ profile will show some dependence on the relative orientation of the defect configuration with respect to scattering vector. To investigate this effect, $J(p_z)$ between elemental Si and a $2B_i^0$ cluster was also calculated along the boron interstitial 'dimer' axis. This modified the shape of $\Delta J(p_z)$, but not its overall magnitude (see supplementary material). Therefore, the experimental $\Delta J(p_z)$ curve in figure 4(a) is not in agreement with theory.

To test the robustness of the experimental data the difference profile due to anisotropy of bonding along [110] and [100] directions, i.e. $\Delta J(p_z) = J(p_z)_{[110]} - J(p_z)_{[100]}$, was calculated for elemental silicon. This was motivated by the fact that both $J(p_z)_{[110]}$ and $J(p_z)_{[100]}$ profiles are extracted from the same specimen, thus keeping experimental variables, such as specimen thickness, as constant as possible. Furthermore,

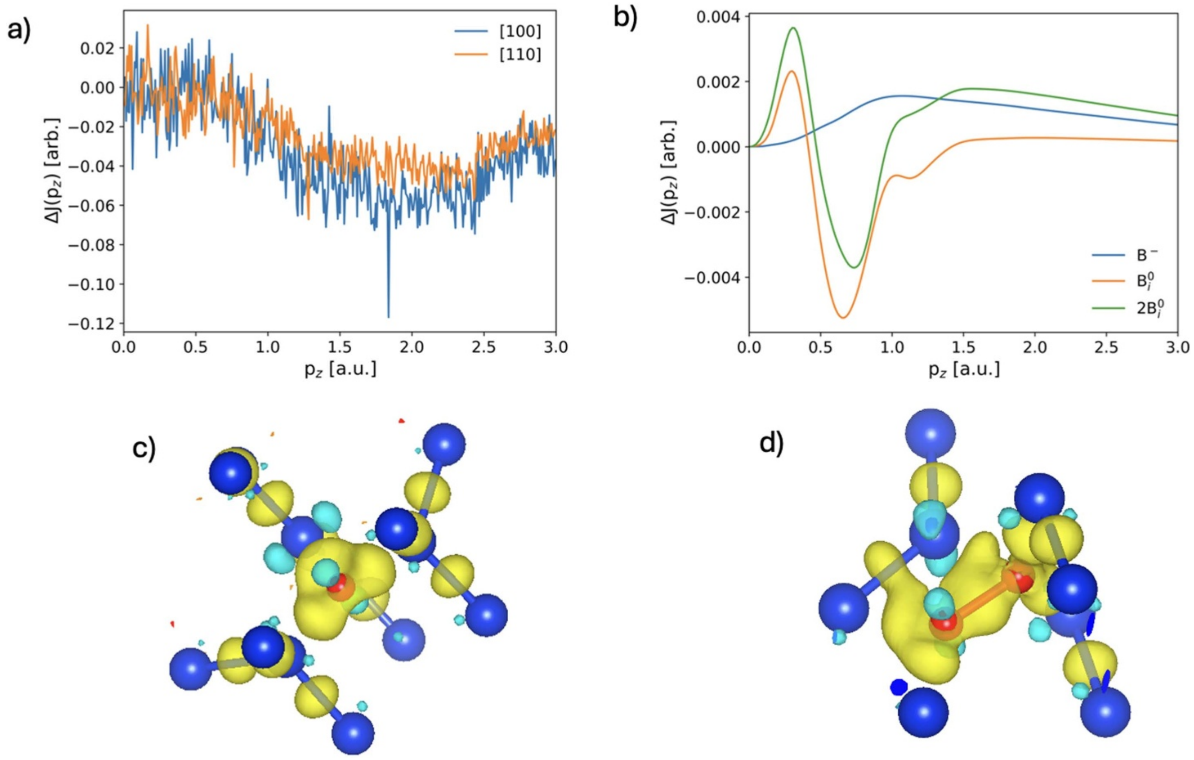

Figure 4. (a) Experimental $\Delta J(p_z)$ difference profiles between elemental Si and boron-doped Si, measured along [100] and [110] directions. (b) DFT simulated $\Delta J(p_z)$ difference profiles between elemental Si and B^-, B_i^0 and $2\mathrm{B}_i^0$ defect configurations, calculated along [100]. (c) is the change in electron density for a B_i^0 interstitial. The red and blue atoms represent boron and silicon, respectively. Yellow represents electron density accumulation due to bonding, while cyan represents a depletion. (d) is the equivalent figure for a $2\mathrm{B}_i^0$ interstitial cluster.

anisotropic Compton profiles for silicon have been extensively studied [51–53] and provide a suitable reference for our data. Figure 5(a) shows the experimental and DFT simulated $\Delta J(p_z)$ profiles superimposed. The $\Delta J(p_z)$ order of magnitude is now in better agreement for both theory and experiment, although the overall shape of the profiles are still different. The finite size of the objective aperture in dark-field Compton EELS measurements is a contributing factor to its shape, since a range of Compton scattering angles are allowed, each with its own Compton peak energy. Bragg diffraction also has a strong influence on the shape of the Compton profile [37, 54]. However, care was taken to minimise any Bragg reflections (section 3), as evidenced by the symmetrical shape of the Compton signal (figure 3(a)). Electron diffraction patterns for the Compton measurements can be found in the supplementary material. Low-energy-loss TDS is nevertheless inevitable and cannot be avoided.

To determine the role of TDS on the Compton profile, $J(p_z)$ for elemental Si at different specimen thicknesses was measured (figure 5(b)). An argon ion-beam milled silicon sample with non-uniform thickness was used for this purpose. Kinematical diffraction conditions were chosen by tilting the specimen away from any zone-axis and by ensuring the Compton scattering vector $\mathbf{q}$ did not align with any low-index crystallographic direction, such as [110] or [100]. The specimen thickness (t) was measured using EELS and expressed as a fraction of the inelastic mean free path (λ). Figure 5(b) shows that $J(p_z)$ broadens with increasing specimen thickness or (t/λ). Further analysis indicated that this broadening is not due to multiple inelastic scattering, provided the specimen is reasonably thin (see Supplementary Material). This is expected, since inelastic scattering is dominated by plasmons, which have a much narrower width than the Compton signal. Instead, the broadening is due to the TDS diffuse intensity background. Compton scattering of the TDS background will contribute a signal that varies as q^{-4}, where q is the scattering vector magnitude [54]. Assuming an approximately constant background intensity, the TDS electrons at smaller q will contribute more strongly to the Compton signal. The Compton peak energy decreases for smaller q, so that with increasing specimen thickness and TDS scattering, the Compton peak position should shift to lower energy loss. This is indeed what is observed experimentally, i.e. the Compton peak energy systematically shifted from 596 eV to 556 eV as the specimen thickness t/λ increased from 0.37 to 1.06 (see Supplementary Material). TDS and objective aperture size are therefore likely to cause the discrepancy in $\Delta J(p_z)$ shape between experiment and theory (figure 5(a)).

In our measurements care was taken to ensure the elemental Si and boron-doped Si specimens had similar thicknesses. Despite this precaution it cannot be guaranteed that the $\Delta J(p_z)$ profile in figure 4(a) is free from residual TDS artefacts. In fact, diffuse scattering due to the crystal lattice strain field surrounding dopant atoms has previously been reported in degenerate boron-doped Si [55]. The diffuse scattered background intensity can therefore have different distributions for

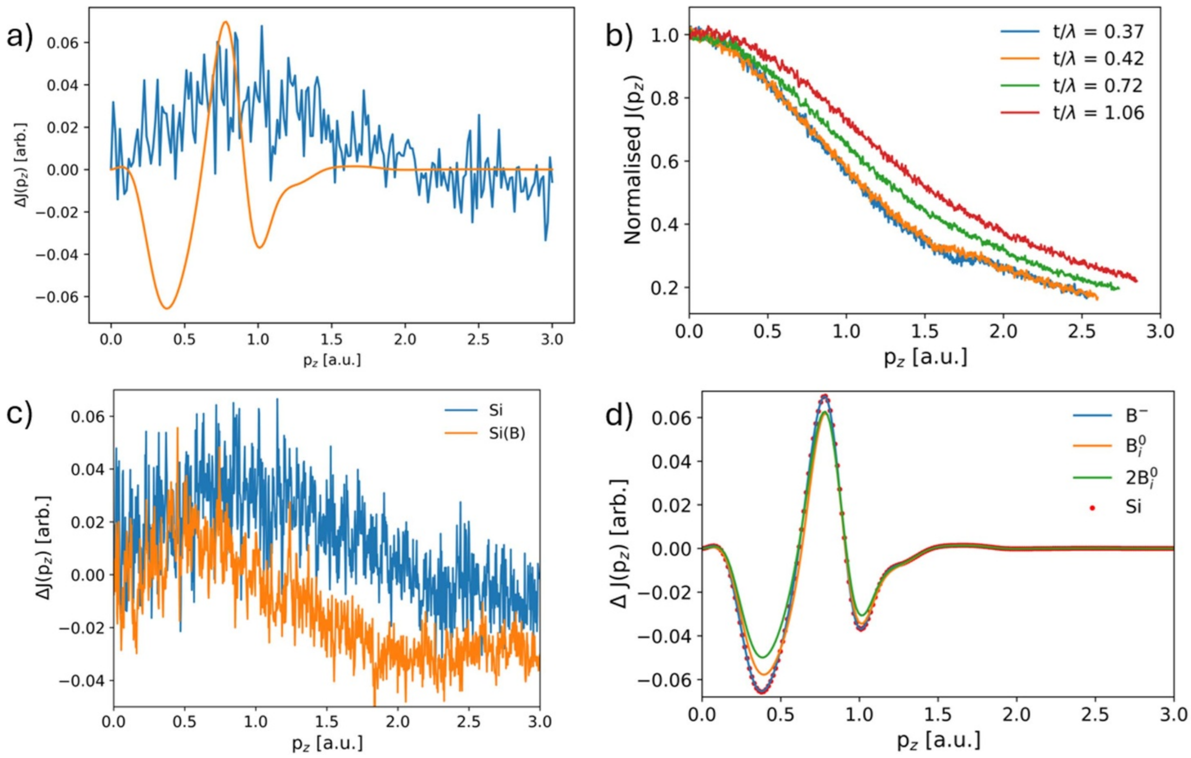

Figure 5. (a) $\Delta J(p_z)$ difference profile due to [110]-[100] bonding anisotropy in elemental Si. DFT (orange) and experimental (blue) data are shown. (b) Experimental $J(p_z)$ profiles for elemental Si extracted from regions of varying thickness (expressed as a t/λ ratio). (c) Experimental $\Delta J(p_z)$ difference profiles due to [110]-[100] bonding anisotropy in elemental Si and boron-doped Si. (d) DFT simulated $\Delta J(p_z)$ difference profiles due to [110]-[100] bonding anisotropy in elemental Si and B^-, B_i^0 and $2B_i^0$ boron defect configurations.

doped and undoped Si. Nevertheless, figure 5(a) suggests that extracting $\Delta J(p_z)$ from the same specimen is a more suitable method of mitigating the diffuse background. Figure 5(c) shows experimental $\Delta J(p_z)$ profiles due to bonding anisotropy along [110] and [100] directions in elemental Si and boron-doped Si. Although noisy, clear systematic differences are observed. For example, the boron-doped Si profile is negative for $p_z > 1$ a.u., while elemental Si is positive for $p_z < 2$ a.u. and slightly negative at larger momentum. The equivalent DFT simulated $\Delta J(p_z)$ profiles for B^- acceptor, B_i^0 interstitial and $2B_i^0$ interstitial cluster are shown in figure 5(d). There is strong overlap between the $\Delta J(p_z)$ profiles for acceptor and elemental Si. However, the difference in $\Delta J(p_z)$ between a $2B_i^0$ cluster and elemental Si is of the same order of magnitude as measured by experiment (figure 5(c)). This suggests that BICs introduce further bonding anisotropy in the silicon host lattice. The anisotropy measured by Compton scattering (figure 5(c)) nevertheless has a different shape to that predicted by theory (figure 5(d)). This is not surprising, since even the bonding anisotropy measured for elemental silicon was distorted by TDS artefacts (figure 5(a)). Furthermore, the DFT simulations only explored a limited subset of boron defect configurations that are likely to be present in the sample.

5. Conclusions

The Hall-measured hole concentration in the degenerately boron-doped Si sample is 10^{20}cm^{-3}. Vibrational EELS revealed a broad defect phonon band centred at $1064\,\text{cm}^{-1}$ wavenumber, significantly above the optical phonon mode for elemental Si. Electron Compton scattering measurements of the $\Delta J(p_z)$ bonding anisotropy along [110] and [100] crystallographic directions showed subtle differences due to boron doping. DFT simulations for defect supercells containing boron acceptors at similarly high concentrations showed very little change in vibrational or electronic properties. Better agreement with experiment was found for DFT supercells containing interstitial clusters. For example, the maximum phonon wavenumber increased with cluster size, provided the packing density within the cluster was reasonably high. Similarly, the bonding anisotropy due to interstitial clusters was of a similar order of magnitude as that observed by experiment. However, the limited energy resolution of monochromated EELS, as well as experimental artefacts from diffuse background scattering in Compton EELS, precluded a precise identification of the type of interstitial cluster configurations present in our sample. DFT calculations indicated that at high boron concentrations, interstitial clusters had a lower formation energy per atom compared to acceptor ions. Interstitial cluster formation is therefore thermodynamically driven and must be taken into account in the design of degenerately boron-doped Si devices. As demonstrated in this study, clustering can have measurable impacts on the phonon and electronic structure of the silicon host lattice. The high spatial resolution of (S)TEM makes EELS a promising technique for investigating clustering phenomena in real devices.

Data availability statement

The data that support the findings of this study are openly available at the following URL/DOI: https://doi.org/10.15128/r1mw22v5500.

Supplementary Material 1 available at https://doi.org/10.1088/1361-648X/ae191e/data1.

Animation 1 available at https://doi.org/10.1088/1361-648X/ae191e/data2.

Animation 2 available at https://doi.org/10.1088/1361-648X/ae191e/data3.

Acknowledgments

K D is financially supported by the National Overseas Scholarship scheme, Ministry of Social Justice and Empowerment, Government of India. S P H is financially supported by the EPSRC Centre for Doctoral Training in Renewable Energy Northeast Universities (ReNU) through Grant EP/SO23836/1. Instrument time at the EPSRC National Research Facility for Advanced Electron Microscopy, SuperSTEM (under Grant Number EP/W021080/1) is gratefully acknowledged. J D M and L J P acknowledge funding from the EPSRC via grant EP/W03445X/1.

ORCID iDs

K Dhamotharan 0000-0002-9999-8928
S Wang 0000-0003-2645-2075
S P Hayes 0009-0009-3989-5247
Q M Ramasse 0000-0001-7466-2283
L J Phillips 0000-0001-5181-1565
J D Major 0000-0002-5554-1985
G Zoppi 0000-0003-3622-6899
B G Mendis 0000-0003-2334-2866

References

[1] Liefting J, Schreutelkamp R, Vanhellemont J, Vandervorst W, Maex K, Custer J and Saris F 1993 Electrically active, ion implanted boron at the solubility limit in silicon *Appl. Phys. Lett.* **63** 1134–6

[2] Solmi S, Landi E and Baruffaldi F 1990 High-concentration boron diffusion in silicon: simulation of the precipitation phenomena *J. Appl. Phys.* **68** 3250–8

[3] Cowern N, Janssen K and Jos H 1990 Transient diffusion of ion-implanted B in Si: dose, time and matrix dependence of atomic and electrical profiles *J. Appl. Phys.* **68** 6191–8

[4] Hofker W, Werner H, Oosthoek D and Koeman N 1974 Boron implantations in silicon: a comparison of charge carrier and boron concentration profiles *Appl. Phys.* **4** 125–33

[5] Collart E *et al* 2000 Cluster formation during annealing of ultra-low-energy boron-implanted silicon *J. Vac. Sci. Technol. B* **18** 435–9

[6] Raghuwanshi M, Lanterne A, Perchec J L, Pareige P, Cadel E, Gall S and Duguay S 2015 Influence of boron clustering on the emitter quality of implanted silicon solar cells: an atom probe tomography study *Prog. Photovolt. Res. Appl.* **23** 1724–33

[7] Tarnow E 1992 Theory of two boron neutral pair defects in silicon *J. Phys.: Condens. Matter* **4** 5405

[8] Zhu J, Rubia T D D, Yang L, Mailhiot C and Gilmer G H 1996 *Ab initio* pseudopotential calculations of B diffusion and pairing in Si *Phys. Rev. B* **54** 4741

[9] Pelaz L, Gilmer G, Gossmann H-J, Rafferty C, Jaraiz M and Barbolla J 1999 B cluster formation and dissolution in Si: a scenario based on atomistic modeling *Appl. Phys. Lett.* **74** 3657–9

[10] Lenosky T J, Sadigh B, Theiss S K, Caturla M-J and de la Rubia T D 2000 *Ab initio* energetics of boron-interstitial clusters in crystalline Si *Appl. Phys. Lett.* **77** 1834–6

[11] Liu X Y, Windl W and Masquelier M P 2000 *Ab initio* modeling of boron clustering in silicon *Appl. Phys. Lett.* **77** 2018–20

[12] Yamauchi J, Aoki N and Mizushima I 2001 Vibrational properties of two boron atoms in silicon *Phys. Rev. B* **63** 073202

[13] Uberuaga B P, Henkelman G, Jonsson H, Dunham S, Windl W and Stumpf R 2002 Theoretical studies of self-diffusion and dopant clustering in semiconductors *Phys. Status Solidi b* **233** 24–30

[14] Chen X, Li L, Wang M, Ren H, Liu X, Zeng G and Yang G 2024 Carrier-induced formation of electrically active boron-interstitial clusters in irradiated boron-doped silicon *J. Appl. Phys.* **135** 055101

[15] Severac F, Cristiano F, Bedel-Pereira E, Fazzini P F, Boucher J, Lerch W and Hamm S 2010 Influence of boron-interstitials clusters on hole mobility degradation in high dose boron-implanted ultrashallow junctions *J. Appl. Phys.* **107** 123711

[16] Bisognin G, De Salvador D, Napolitani E, Carnera A, Bruno E, Mirabella S, Priolo F and Mattoni A 2006 Lattice strain induced by boron clusters in crystalline silicon *Semicond. Sci. Technol.* **21** L41

[17] Kohn W 1999 Electronic structure of matter-wave functions and density functionals *Rev. Mod. Phys.* **71** 1253–66

[18] Hohenberg P and Kohn W 1964 Density functional theory (DFT) *Phys. Rev.* **136** B864

[19] Hage F S, Nicholls R J, Yates J R, McCulloch D G, Lovejoy T C, Dellby N, Krivanek O L, Refson K and Ramasse Q M 2018 Nanoscale momentum-resolved vibrational spectroscopy *Sci. Adv.* **4** eaar7495

[20] Williams B and Thomas J 1983 Compton scattering as a technique for the study of solids *Int. Rev. Phys. Chem.* **3** 39–82

[21] Feng Z, Zhang X, Sakurai Y, Wang Z, Li H and Hu H 2019 Compton profile of few-layer graphene investigated by electron energy-loss spectroscopy *Sci. Rep.* **9** 17313

[22] Talmantaite A, Xie Y, Cohen A, Mohapatra P, Ismach A, Mizoguchi T, Clark S and Mendis B 2023 Twist-induced interlayer charge buildup in a WS_2 bilayer revealed by electron Compton scattering and density functional theory *Phys. Rev. B* **107** 235424

[23] Isaacs E, Shukla A, Platzman P, Hamann D, Barbiellini B and Tulk C 2000 Compton scattering evidence for covalency of the hydrogen bond in ice *J. Phys. Chem. Solids* **61** 403–6

[24] Payne M C, Teter M P, Allan D C, Arias T and Joannopoulos J 1992 Iterative minimization techniques for *ab initio* total-energy calculations: molecular dynamics and conjugate gradients *Rev. Mod. Phys.* **64** 1045

[25] Clark S J, Segall M D, Pickard C J, Hasnip P J, Probert M I J, Refson K and Payne M C 2005 First principles methods using CASTEP *Z. Kristallogr. Cryst. Mater.* **220** 567–70

[26] Rappe A M, Rabe K M, Kaxiras E and Joannopoulos J 1990 Optimized pseudopotentials *Phys. Rev. B* **41** 1227

[27] Lin J, Qteish A, Payne M and Heine V 1993 Optimized and transferable nonlocal separable *ab initio* pseudopotentials *Phys. Rev. B* **47** 4174

[28] Perdew J P and Zunger A 1981 Self-interaction correction to density-functional approximations for many-electron systems *Phys. Rev. B* **23** 5048

[29] Monkhorst H J and Pack J D 1976 Special points for brillouin-zone integrations *Phys. Rev. B* **13** 5188

[30] Zhang S B and Northrup J E 1991 Chemical potential dependence of defect formation energies in GaAs: Application to Ga self-diffusion *Phys. Rev. Lett.* **67** 2339–42

[31] Refson K, Tulip P R and Clark S J 2006 Variational density-functional perturbation theory for dielectrics and lattice dynamics *Phys. Rev. B* **73** 155114

[32] Schattschneider P, Pongratz P and Hohenegger H 1990 Compton scattering in electron energy loss spectrometry *Scanning Microsc.* **1990** 4

[33] Olevano V, Titov A, Ladisa M, Hämäläinen K, Huotari S and Holzmann M 2012 Momentum distribution and Compton profile by the *ab initio* GW approximation *Phys. Rev. B* **86** 195123

[34] Biggs F, Mendelsohn L and Mann J 1975 Hartree-Fock Compton profiles for the elements *At. Data Nucl. Data Tables* **16** 201–309

[35] Krivanek O L, Ursin J P, Bacon N J, Corbin G J, Dellby N, Hrncirik P, Murfitt M F, Own C S and Szilagyi Z S 2009 High-energy-resolution monochromator for aberration-corrected scanning transmission electron microscopy/electron energy-loss spectroscopy *Phil. Trans. R. Soc. A* **367** 3683–97

[36] Hage F S, Radtke G, Kepaptsoglou D M, Lazzeri M and Ramasse Q M 2020 Single-atom vibrational spectroscopy in the scanning transmission electron microscope *Science* **367** 1124–7

[37] Mendis B G and Talmantaite A 2022 Towards electron energy loss Compton spectra free from dynamical diffraction artifacts *Microsc. Microanal.* **28** 1971–80

[38] Williams D B and Carter C B 1996 *Transmission Electron Microscopy* (Springer)

[39] Schattschneider P and Exner A 1995 Progress in electron Compton scattering *Ultramicroscopy* **59** 241–53

[40] Mendis B 2022 Background subtraction in electron Compton spectroscopy *Micron* **163** 103363

[41] Talmantaite A, Hunt M and Mendis B 2020 Electron compton scattering and the measurement of electron momentum distributions in solids *J. Microsc.* **279** 185–8

[42] Montroll E W and Potts R B 1955 Effect of defects on lattice vibrations *Phys. Rev.* **100** 525–43

[43] Egerton R F 2011 *Electron Energy-Loss Spectroscopy in the Electron Microscope* 3rd edn (Springer)

[44] Pizzini S, Acciarri M and Binetti S 2005 From electronic grade to solar grade silicon: chances and challenges in photovoltaics *Phys. Status Solidi a* **202** 2928–42

[45] Bohling C and Sigmund W 2016 Self-limitation of native oxides explained *Silicon* **8** 339–43

[46] Pai P G, Chao S S, Takagi Y and Lucovsky G 1986 Infrared spectroscopic study of SiO_x films produced by plasma enhanced chemical vapor deposition *J. Vac. Sci. Technol. A* **4** 689–94

[47] Ibach H, Bruchmann H D and Wagner H 1982 Vibrational study of the initial stages of the oxidation of Si(111) and Si(100) surfaces *Appl. Phys. A* **29** 113–24

[48] Deák P, Gali A, Sólyom A, Ordejón P, Kamarás K and Battistig G 2003 Studies of boron–interstitial clusters in Si *J. Phys.: Condens. Matter* **15** 4967

[49] Adey J, Goss J P, Jones R and Briddon P R 2003 Identification of boron clusters and boron-interstitial clusters in silicon *Phys. Rev. B* **67** 245325

[50] Martin A V, Findlay S D and Allen L J 2009 Model of phonon excitation by fast electrons in a crystal with correlated atomic motion *Phys. Rev. B* **80** 024308

[51] Reed W and Eisenberger P 1972 Gamma-ray Compton profiles of diamond, silicon and germanium *Phys. Rev. B* **6** 4596 http://10.1098/rspa.1987.0011

[52] Seth A and Ellis D 1977 Momentum densities and Compton profiles of diamond, silicon and silicon carbide *J. Phys. C: Solid State Phys.* **10** 181

[53] Delaney P, Králik B and Louie S G 1998 Compton profiles of Si: Pseudopotential calculation and reconstruction effects *Phys. Rev. B* **58** 4320

[54] Williams B, Uppal M and Brydson R 1987 Dynamical scattering effects in electron scattering measurements of the Compton profiles of solids *Proc. R. Soc. A* **409** 161–76

[55] Perovic D, Rossouw C and Howie A 1993 Imaging elastic strains in high-angle annular dark field scanning transmission electron microscopy *Ultramicroscopy* **52** 353–9